Collimator Design for a Brain SPECT/MRI Insert

Debora Salvado, *Student Member, IEEE*, Kjell Erlandsson, Alexandre Bousse, Michele Occhipinti, Paolo Busca, Carlo Fiorini, *Senior Member, IEEE*, Brian F. Hutton, *Senior Member, IEEE*, and the INSERT collaboration

***Abstract*—This project's goal is to design a SPECT insert for a clinical MRI system for simultaneous brain SPECT/MR imaging, with a high-sensitivity collimator and high-resolution detectors. We have compared eight collimator designs, four multi-pinhole and four multi-slit slit-slat configurations. The collimation was designed for a system with 2 rings of 25 5×5 cm detectors. We introduce the concept of 1/2-pinhole and 1/2-slit, which are transaxially shared between two adjacent detectors. Analytical geometric efficiency was calculated for an activity distribution corresponding to a human brain and a range of intrinsic detector resolutions R_i and target resolutions R_t at the centre of the FOV. Noise-free data were simulated with and without depth-of-interaction (DOI) information, 0.8 mm R_i and 10 mm R_t FWHM, and reconstructed for uniform, Defrise, Derenzo, and Zubal brain phantoms. Comparing the multi-pinhole and multi-slit slit-slat collimators, the former gives better reconstructed uniformity and transaxial resolution, while the latter gives better axial resolution. Although the 2×2-pinhole and 2-slit designs give the highest sensitivities, they result in a sub-optimal utilisation of the detector FOV. The best options are therefore the $5{+}2\ 1/2$-pinhole and the $1{+}2\ 1/2$-slit systems, with sensitivities of 1.8×10^{-4} and 3.2×10^{-4}, respectively. Noiseless brain phantom reconstructions with the multi-pinhole collimator are slightly superior as compared to slit-slat, in terms of symmetry and accuracy of the activity distribution, but the same is not true when noise is included. DOI information reduces artefacts and improves uniformity in geometric phantoms. Further evaluation is needed with prototype collimators.**

***Index Terms*—Collimator design, multi-modality, pinhole, slit-slat, SPECT insert, stationary system.**

I. Introduction

A SIMULTANEOUS SPECT/MR system could provide combined functional (SPECT and MRI) and morphological information (MRI), correlated in space and time. SPECT provides the possibility to target different biomarkers using multiple radionuclides simultaneously, and to label compounds with either diagnostic or therapeutic radionuclides. Therefore it has the potential to estimate internal radiation dose, important for the treatment planning of personalised radionuclide-based therapies. MRI provides the spatial resolution for accurate localisation, but also functional information by applying various MRI pulse-sequences.

Some pre-clinical SPECT/MRI systems have already been developed [1], [2], although these are not truly integrated. More recently, studies addressing simultaneous SPECT/MRI have shown the feasibility of these multi-modality systems for preclinical use [3]–[5].

The objective of this paper is to design a SPECT insert for a clinical MRI system in order to perform simultaneous brain SPECT/MR imaging in humans. Previous work shows preliminary results on resolution and sensitivity and demonstrate that rotation can be avoided [6]. Each detector unit of the double-ring insert will consist of an 8 mm-thick CsI:Tl crystal and SiPM-based readout of size $50 \times 50 \times 13.69$ mm, insensitive to magnetic fields, with expected intrinsic resolution of 0.8 mm and a dead space of 5 mm around the edge [7]. Compactness is needed due to the limited space inside the MR bore, whose internal diameter is 59 cm. The external diameter of the SPECT insert must be less than 44.5 cm because it will be positioned on top of the patient bed and the internal diameter should not be less than 33 cm to accommodate the patient head and the MRI receive/transmit coil (Fig. 1). The system has to be stationary for practical reasons and to minimise interference with

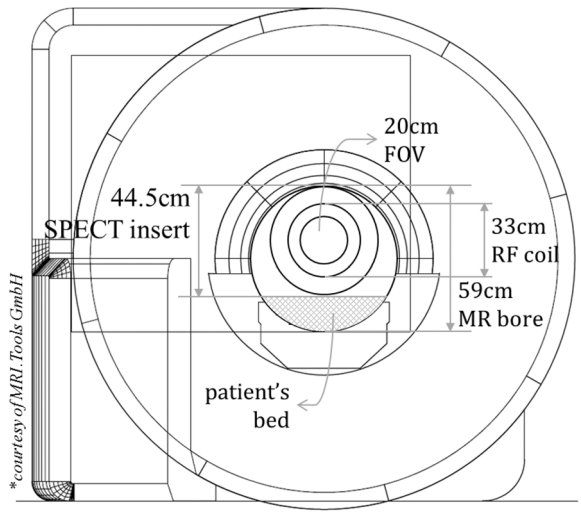

Fig. 1. Technical sketch of the mMR installed at the UCLH. The main dimensions of the MR bore and SPECT insert are specified in cm. [mMR courtesy of MRI. Tools GmbH].

Manuscript received August 29, 2014; revised December 19, 2014; accepted June 11, 2015. Date of publication August 06, 2015; date of current version August 14, 2015. D Salvado was supported by a Ph.D. Fellowship (SFRH/BD/88093/2012) by the Portuguese national funding agency for science, research and technology (FCT). This work was done as part of the INSERT collaboration supported by EC under the FP7-HEALTH program (305311). UCL/UCLH research was supported by the NIHR University College London Hospitals Biomedical Research Centre.

D. Salvado, K. Erlandsson, and A. Bousse are with the Institute of Nuclear Medicine, University College London, London W1E 6BT, U.K. (e-mail: debora.salvado.12@ucl.ac.uk).

M. Occhipinti, P. Busca, and C. Fiorini are with Politecnico di Milano-Dipartimento di Elettronica, Informazione e Bioingegneria, 20133 Milano, Italy, and also with INFN, Sezione di Milano, 20133 Milano, Italy.

B. F Hutton is with the Institute of Nuclear Medicine, University College London, London W1E 6BT, U.K., and also with the Centre for Medical Radiation Physics, University of Wollongong, Sydney, Australia.

Digital Object Identifier 10.1109/TNS.2015.2450017

the MRI system. Stationary multi-pinhole systems have been investigated previously by several groups [8]–[13].

The main limitations in the development of the collimation system are the restricted space and the limited angular sampling. Therefore we discuss the collimator design and suggest possible solutions for these issues with a simultaneous brain SPECT/MR. This work is part of the INSERT project (http://www.insert-project.eu/).

II. Methods

The evaluation of different collimator designs focused on the trade-off between sensitivity and spatial resolution, the space constraints due to the MR system, and the limited angular sampling due to the need for a stationary system.

The slit-slat collimator was included in the evaluation due to its suitability for brain imaging [14]. This collimator provides two different types of collimation in the transaxial and axial directions. In most applications of slit-slat collimators, there is magnification in the transaxial direction defined by the slit. In our system, the distance between the collimator and the detector is small so that the SPECT insert can fit inside the MRI system and the imaging FOV is large in comparison to the detector size. Hence minification will occur in the projections space; however the system can benefit from the detector's high intrinsic resolution to compensate for this effect. In order to improve sensitivity, also multi-slit configurations of the slit-slat collimator were evaluated, and compared to analogous multi-pinhole collimator configurations.

In order to improve angular sampling with pinhole collimators, the two detector rings were rotated by half the detector-size. This mismatched configuration of the detector rings doubles the number of views as each detector ring can cover the entire axial FOV (Fig. 2). For multi-slit slit-slat configurations with parallel slats, each ring covers only half of the imaging FOV, resulting in a small axial gap due to the 5 mm dead area at the edge of the detectors (Fig. 3) and a smaller axial FOV compared to multi-pinhole systems: we assume an ellipsoidal imaging FOV of size $20 \times 20 \times 15$ cm for the pinhole collimators due to the diverging geometry and a cylindrical FOV of size $20 \times 20 \times 10$ cm for the slit-slat collimators. Note that for multi-pinhole configurations, the axial gap is not a problem because the whole FOV is projected onto each detector. Additionally we propose the use of half-pinholes or half-slits to improve angular sampling. These half apertures have only half the projection area of a complete pinhole/slit and are shared between adjacent detectors in a ring. Therefore, in practice, the two halves form a complete pinhole/slit when the detectors are arranged in a ring configuration.

The use of pinholes and slits for collimation can introduce parallax errors due to photons incident with an oblique angle with respect to the crystal. These can be reduced using depth-of-interaction (DOI) information. For DOI it is assumed that the crystal's first and second half can be differentiated, ie. two separate detector-layers, based on the distribution of scintillation light, reducing the associated detection-position uncertainty (Fig. 4).

Geometrical optimisation was performed using the inequality in Eq. (1) to obtain the maximum number of detectors N in a ring that fits between the patient bed and MRI bore.

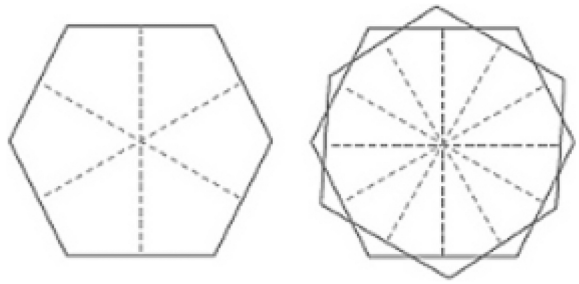

Fig. 2. Angular sampling for matched (left) and mismatched (right) detector rings. Dashed lines correspond to the number of angular views. NB: Only six detectors are shown here for clarity.

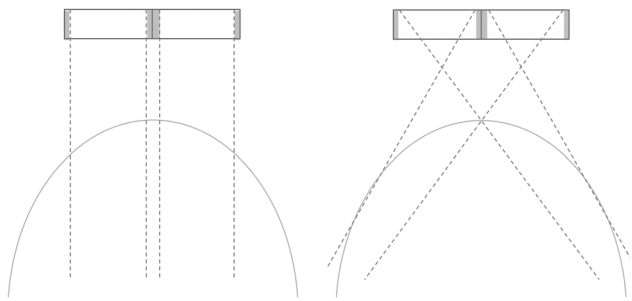

Fig. 3. Detector's dead area (shaded area). The dashed lines represent the axial projection for the single-pinhole (right) and the slit-slat (left) collimators.

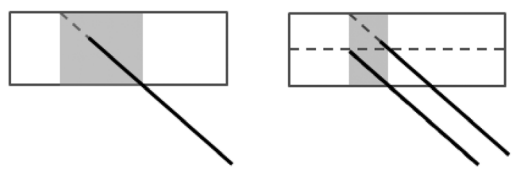

Fig. 4. Parallax error (left) and improvement (right) using DOI information. For the incident photon, the uncertainty in the detection point is represented by the shaded area. The horizontal dashed line divides the crystal in two halves.

$$2\sqrt{W_{\mathrm{det}}^2 + \left(\frac{W_{\mathrm{det}}}{\tan\left(\frac{\pi}{N}\right)} + L_{\mathrm{det}}\right)^2} < d_{\mathrm{MRbore}}, N \in \mathbb{N} \quad (1)$$

where L_{det} is the height of the detector; W_{det} is half of the detector width; d_{MRbore} is the maximum outer diameter of the SPECT insert in order for it to fit inside the MR bore; and $\theta_1 = \pi/N$ is half the angle covered by one detector (see Fig. 5). Solving for N, we obtained a maximum of 25 detectors per ring.

Fig. 6 and Fig. 7 show possible configurations of multi-pinhole and multi-slit slit-slat collimators, respectively, for the SPECT insert, with two rings of 25 detectors each. Fig. 8 and Fig. 9 show the collimator configurations that apply the half pinhole/slit concept: the $5+2\cdot1/2$-pinhole and the $1+2\cdot1/2$-slit slit-slat, respectively. Because they have half-pinholes or half-slits, the $5 + 2 \cdot 1/2$-pinhole and $1 + 2 \cdot 1/2$-slit configurations can be considered intermediate between the 2×2- and 3×3-pinhole and 2- and 3-slit slit-slat collimators, respectively. One advantage of these configurations in comparison to the 2×2-pinhole and 2-slit ones is that they make better use of

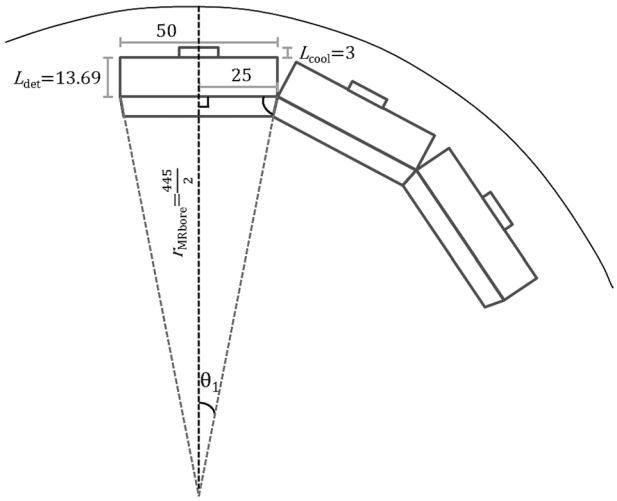

Fig. 5. Partial diagram of a detection ring. The outer circumference represents the MR bore opening and the boxes, the scintillation crystal, the detector and the cooling system (from inside to outside). L_{det} and L_{cool} are the heights of the detector and the cooling system, respectively. Dimensions are given in mm (figure not to scale).

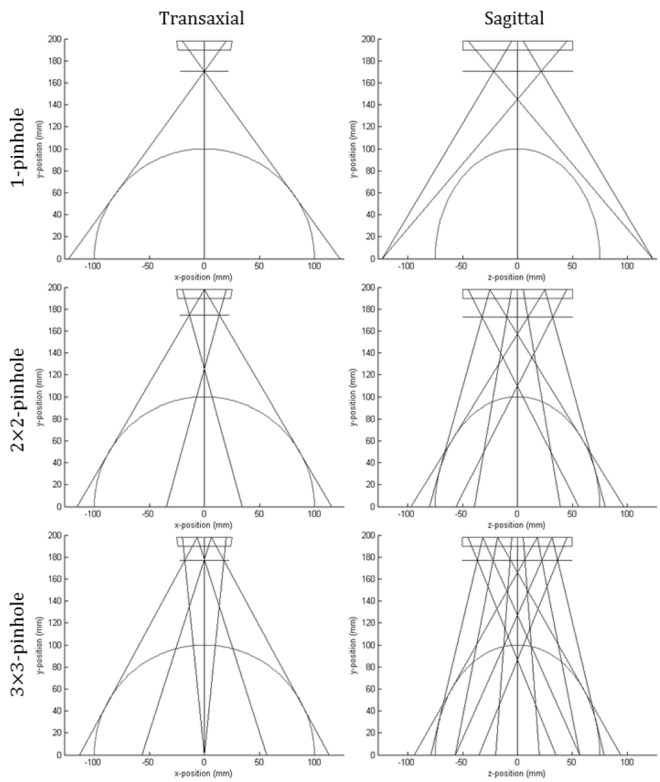

Fig. 6. Diagrams of the multi-pinhole collimator configurations, single (1st row), 2×2 (2nd row) and 3×3 (3rd row) pinholes per detector, for transaxial and sagittal views. The lines correspond to the projection of the pinholes FOV.

the central part of the detectors. With the 2×2-pinhole and the 2-slit slit-slat collimators, the centre of the detectors, which is the best part, would be used to image the edges of the object FOV, where there is usually not much activity. In addition, the slit-slat configurations have extended slats - extending from the scintillation crystal to the RF coil. As the resolution is fixed in both directions, the slat spacing can be increased, improving sensitivity. When the slat spacing increases, the shielding effect

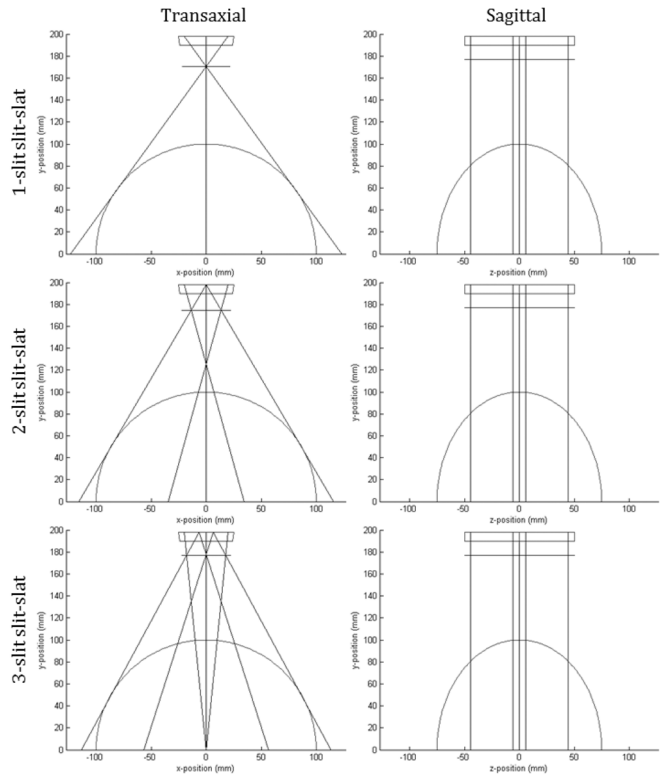

Fig. 7. Diagrams of the multi-slit slit-slat collimator configurations, 1 (1st row), 2 (2nd row) and 3 (3rd row) slits per detector, for transaxial and sagittal views. The lines correspond to the projection of the slits FOV. The collimator slats are parallel, hence they correspond to straight projections in the sagittal view.

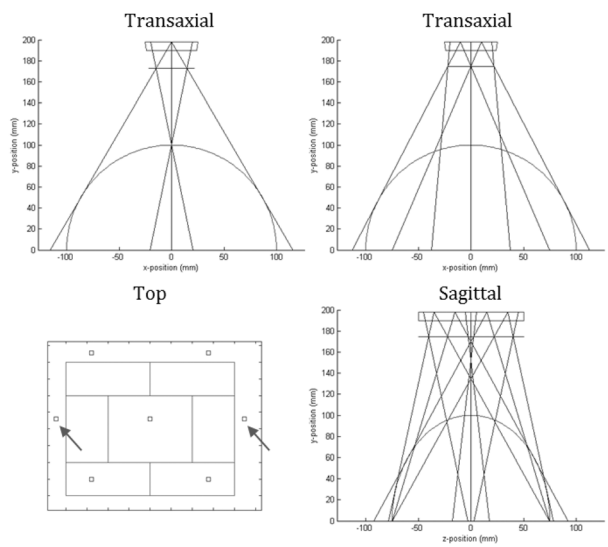

Fig. 8. Diagram of the $5 + 2 \cdot 1/2$-pinhole collimator. The half-pinholes are indicated by the arrows. The top row shows transaxial views through the 2-pinhole plane (left) and the $1 + 2 \cdot 1/2$-pinhole plane (right), the bottom left row, the top view, and the bottom right, the sagittal view. In the top view, there is a gap between the projected fields-of-view of the square pinholes and the detector edges, corresponding to the dead space.

of the slats decreases, leading to higher sensitivity for the same acceptance angle.

For all collimator configurations, the geometric efficiency for a given voxel i, pinhole/slit j and detector k was calculated

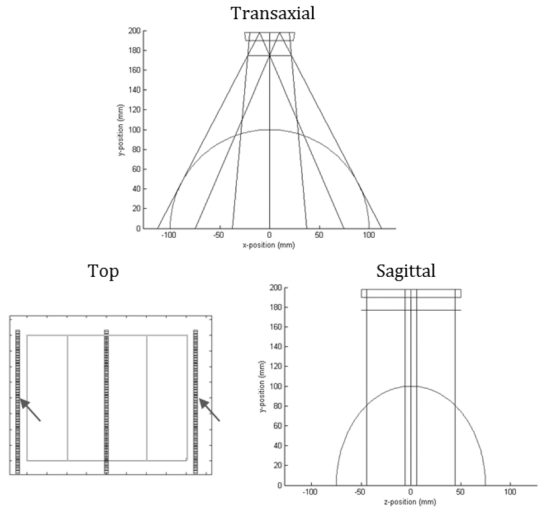

Fig. 9. Diagram of the $1 + 2 \cdot 1/2$-slit slit-slat collimator. The half-slits are highlighted by the arrows. The top row shows a transaxial view, the bottom left, the top view, and the bottom right, the sagittal view. The shaded areas correspond to the slit or half-slit.

using Eq. (2) [15], [16] for the pinhole and slit-slat collimators, respectively. The parameters are the following: h is the distance to the collimator aperture; ϕ is the angle between the incident ray and the pinhole plane; θ is the angle between the incident ray and the aperture slit plane; d is the slat spacing; t is the slat thickness; and l_{Eff} is the slat length corrected for septal penetration. The pinhole/slit aperture w is calculated according to the target resolution with resolution-effective formulae and corrected for septal penetration with sensitivity-effective formulae [17]–[19], considering a tungsten collimator ($\mu = 3.3976\,\mathrm{mm}^{-1}$ at 140.5 keV). Calculations were performed for an intrinsic resolution of the detector of $R_i = 0.8$ mm and different target resolutions $R_t = \{10, 11, 12\}$ mm at the centre of the FOV, as well as a target resolution of $R_t = 10$ mm and different intrinsic resolutions $R_i = \{0.6, 0.8, 1.0\}$ mm, for a double ring of 25 detectors each. Note that for slit-slat configurations, transaxial and axial resolutions were matched to achieve the same target resolution in both directions. The efficiency was averaged over an ellipsoidal volume δ of size $13 \times 18 \times 13$ cm, as shown in Eq. (2).

$$g = \frac{1}{\delta N} \sum_{i \in \delta} \sum_{k \in N} \sum_{j \in n} g_{i,j,k}, \text{ where}$$
$$g_{i,j,k} = \begin{cases} \frac{w^2_{g_{Eff}}}{4\pi h^2} \sin^3 \phi, & \text{pinhole (square hole)} \\ \frac{d^2 w_{g_{Eff}}}{4\pi l_{Eff} h(d+t)} \sin^3 \theta, & \text{slit} - \text{slat} \end{cases} \quad (2)$$

Noise-free data were simulated with 0.8 mm R_i and 10 mm R_t and projected using an angular blurring approach [20]. It can be described as analytical blurring of the line integrals within a cone of response, based on an angular point spread function, allowing for the modelling of a range of collimators by simply changing a weighting function. We used four different phantoms to evaluate uniformity, axial and transaxial sampling issues, and

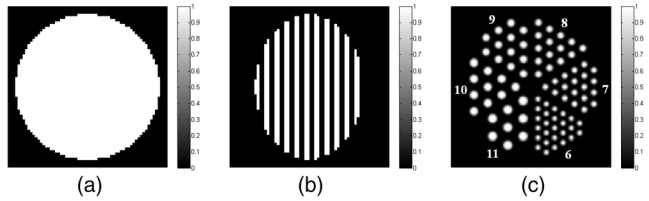

Fig. 10. Geometric phantoms: transaxial section of the (a) uniform phantom, axial section of the (b) Defrise phantom with alternating hot-cold transaxial 6.25 mm-thick compartments, and transaxial section of the (c) Derenzo phantom with 6-11 mm hot rod sources.

TABLE I
RECONSTRUCTION PARAMETERS FOR EACH TYPE OF PHANTOM

Phantom	Phantom matrix size	Phantom voxel size (mm)	Image matrix size	Image voxel size (mm)	Number of iterations	Number of subsets
Uniform	64	3.125	64	3.125	200	5
Defrise	64	3.125	64	3.125	500	5
Derenzo	100	2	64	3.125	400	5
Zubal	90	2.2	64	3.125	400	1

a realistic activity distribution: one phantom with a uniform distribution (Fig. 10(a)); a Defrise phantom with alternating hot and cold transaxial slices of 6.25 mm thickness (Fig. 10(b)); a Derenzo phantom with six segments with hot rod-sources of diameters 6, 7, 8, 9, 10, 11 mm (Fig. 10(c)). All phantoms had an overall ellipsoidal shape with dimensions of $18 \times 18 \times 13.5$ cm. Data were simulated with and without DOI information, corresponding to whether the interaction took place in the first or second half of the crystal, so as to investigate how useful this information could be. Neither attenuation nor scatter was included in the simulations. Images were reconstructed using the ordered subsets expectation maximisation (OSEM) algorithm [21], based on the same projection algorithm. The reconstruction parameters for each phantom are shown in Table I and the specific collimator parameters in Table II and Table III. The reason for not including noise was to better illustrate sampling artefacts.

Simulations were also performed with a Zubal brain phantom [22] (Fig. 20- top row), corresponding to a 30 min acquisition, with 5.5 M counts for the $5+2\cdot1/2$-pinhole and 8.6 M for the $1+2\cdot1/2$-slit slit-slat collimator. Attenuation was included, but no DOI information. Images were reconstructed with 400 iterations of ML-EM. For the noisy simulations, Poisson distributed data were generated based on the forward-projected mean values and smoothed post-reconstruction with a 6 mm 3D Gaussian filter.

III. RESULTS

Fig. 11 and Fig. 12 show the average geometric efficiency for different pinhole and slit-slat configurations, at different target resolutions and intrinsic resolutions of the detectors, respectively. The 2×2-pinhole and 2-slit slit-slat configurations achieve the highest efficiency, for the range of target and intrinsic resolutions shown. Comparing each pinhole configuration with the corresponding slit-slat, the latter achieves higher efficiency. For the 3×3-pinhole and 3-slit slit-slat configurations, there is no efficiency value for an intrinsic resolution of 1.0 mm and a target resolution of 10 mm because it is not possible to obtain a real aperture.

TABLE II
PARAMETERS OF THE PINHOLE DESIGNS FOR $R_t = 10$ AND $R_i = 0.8$ mm

Configuration	2×2	5+2·½	3×3
f [mm]	25.32	23.25	20.77
w [mm]	0.68	0.55	0.28
p_{tr_1}; p_{ax_1} [mm]	-14.83; -15.63	-13.62; -22.65	-17.90; -18.47
	14.83; -15.63	13.62; -22.65	0; -18.47
	-14.83; 7.03	-22.06; -02.94	17.90; -18.47
	14.83; 7.03	0; -02.94	-17.90; -02.62
		22.06; -02.94	0; -02.62
		-13.62; 15.06	17.90; -02.62
		13.62; 15.06	-17.90; 11.6
			0; 11.6
			17.90; 11.6
α_{tr_1}; α_{ax_1} [°]	42; 41	46; 34	34; 34
	42; 41	46; 34	36; 34
	42; 43	22; 35	34; 34
	42; 43	47; 35	34; 35
		22; 35	36; 35
		46; 35	34; 35
		46; 35	34; 35
			36; 35
			34; 35
p_{tr_2}; p_{ax_2} [mm]	-14.83; -07.03	-13.62; -15.06	-17.90; -11.60
	14.83; -07.03	13.62; -15.06	0; -11.60
	-14.83; 15.63	-22.06; 02.94	17.90; -11.60
	14.83; 15.63	0; 02.94	-17.90; 02.62
		22.06; 02.94	0; 02.62
		-13.62; 22.65	17.90; 02.62
		13.62; 22.65	-17.90; 18.47
			0; 18.47
			17.90; 18.47
α_{tr_2}; α_{ax_2} [°]	42; 43	46; 35	34; 35
	42; 43	46; 35	36; 35
	42; 41	22; 35	34; 35
	42; 41	47; 35	34; 35
		22; 35	36; 35
		46; 34	34; 35
		46; 34	34; 34
			36; 34
			34; 34

f = focal length
w = pinhole aperture
p = pinhole position
α = pinhole opening angle
tr and ax refer to the transaxial and axial directions
1 and **2** refer to the detector ring

TABLE III
PARAMETERS OF THE SLIT-SLAT DESIGNS FOR $R_t = 10$, $R_i = 0.8$ mm

Configuration	2-slit	1+2·½-slit	3-slit
f [mm]	25.32	23.25	20.77
d [mm]	1.29	1.29	1.29
t [mm]	0.3	0.3	0.3
l [mm]	24.9	24.9	24.9
w [mm]	0.68	0.55	0.28
p_{tr} [mm]	-14.83	-22.06	-17.90
	14.83	0	0
		22.06	17.90
α_{tr} [°]	42	22	34
	42	47	36
		22	34

f = focal length
d = slat spacing
t = slat thickness
l = slat length
w = slit aperture
p = slit position
α = slit opening angle
tr = transaxial direction

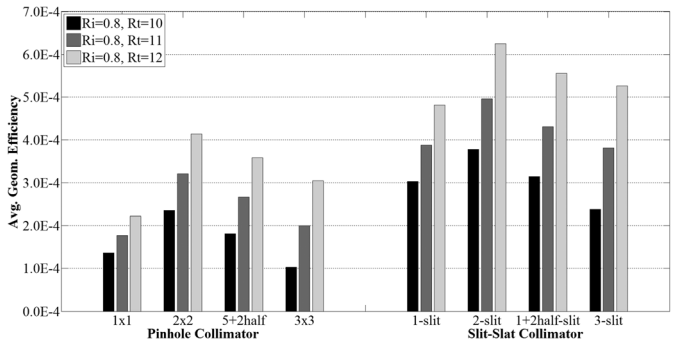

Fig. 11. Plot of the average geometric efficiency G at a fixed intrinsic resolution $R_i = 0.8$ mm for different pinhole and slit-slat configurations and different target resolutions $R_t = \{10, 11, 12\}$ mm.

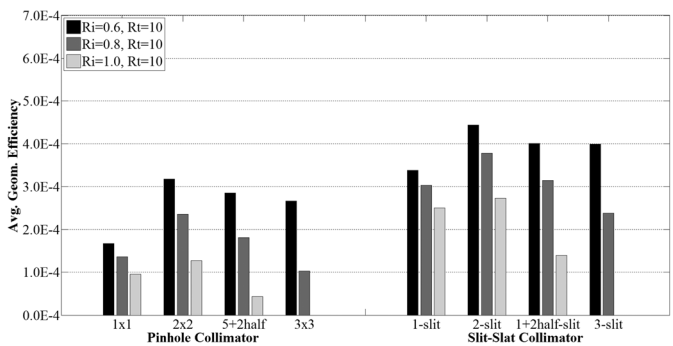

Fig. 12. Plot of the average geometric efficiency G at a fixed target resolution $R_t = 10$ mm for different pinhole and slit-slat configurations and different intrinsic resolutions of the detector $R_i = \{0.6, 0.8, 1\}$ mm.

Fig. 13 and Fig. 14 show the reconstructed images simulated with and without DOI information for the uniform phantom with the different multi-pinhole and multi-slit slit-slat collimator configurations, respectively. These images are averaged over 50 mm axially for display purposes. They show ring and streak artefacts, that are improved when including the DOI information. Ring artefacts near the edges of the phantom are due to the classic Gibbs-effect, related to resolution recovery during reconstruction. The results for the single-pinhole and single-slit slit-slat collimators are not shown due to lack of sampling information for the reconstruction. They also have the lowest efficiency of all the collimator configurations and are therefore excluded from all the phantom simulations.

In order to quantitatively compare the different reconstructions with the uniform phantom, Fig. 15 shows the coefficient of variation (CoV) for each collimator configuration. The inclusion of the DOI information improves significantly the reconstructed uniformity in the case of the multi-slit slit-slat collimators. With DOI, the uniformity improves with increasing number of slits due to improved angular sampling. The deterioration in uniformity for the 3-slit collimator without DOI is due to an increased amount of cross-talk, related to the parallax effect. For the multi-pinhole configurations, the effect of including the DOI information is not obvious. The angular sampling is better with the pinhole collimators due to the angular offset of the two rings,

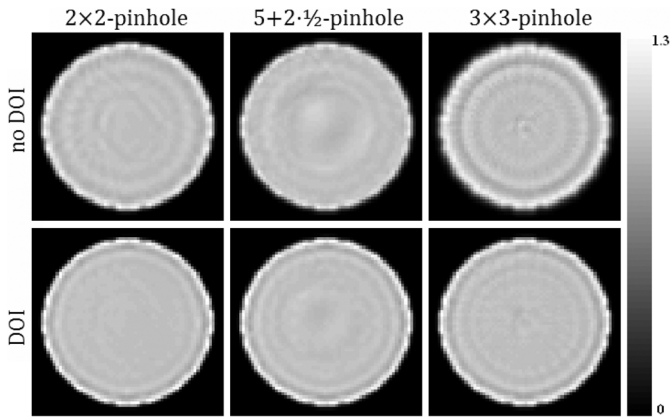

Fig. 13. Reconstructed images for the uniform phantom simulated with different configurations of the pinhole collimator, with (bottom row) and without (top row) DOI information.

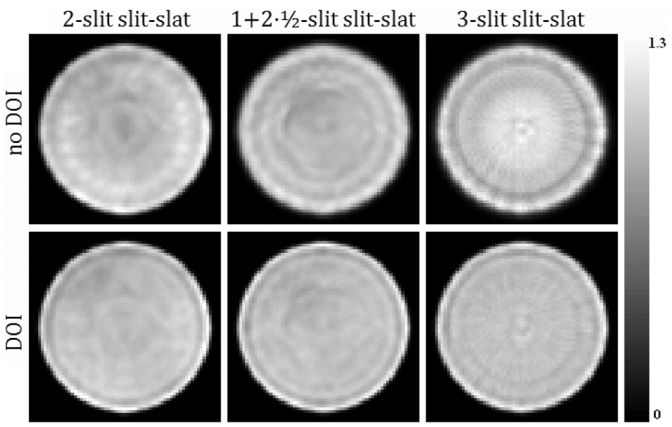

Fig. 14. Reconstructed images for the uniform phantom simulated with different configurations of the slit-slat collimator, with (bottom row) and without (top row) DOI information.

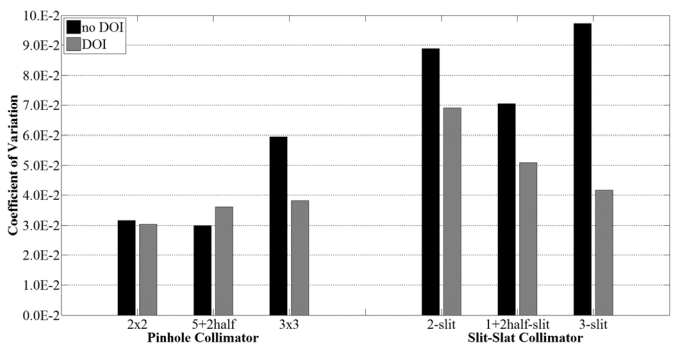

Fig. 15. Plot of the coefficient of variation CoV of the uniform phantom for different pinhole and slit-slat configurations, including and excluding the DOI information from the simulation.

which results in better uniformity compared to the slit-slat collimators. An improvement with DOI can be seen for the 3×3-pinhole collimator for the same reason as above.

Fig. 16 and Fig. 17 show the reconstructed images simulated with and without DOI information for the Defrise phantom, with different multi-pinhole and multi-slit slit-slat configurations, respectively. These images are averaged over 6.25 mm transaxially for display purposes. The contrast between hot and cold

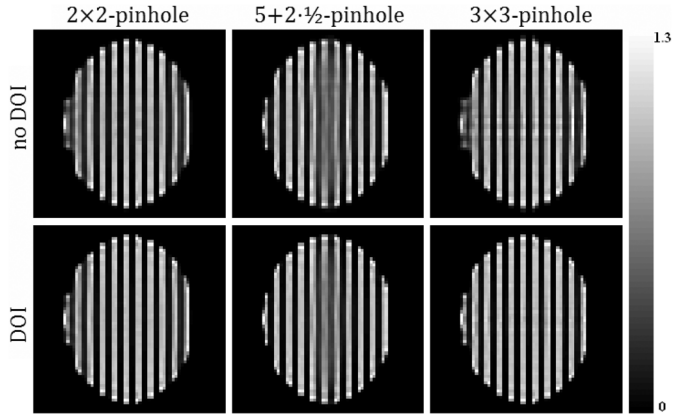

Fig. 16. Reconstructed images for the Defrise phantom simulated with different configurations of the pinhole collimator, with (bottom row) and without (top row) DOI information.

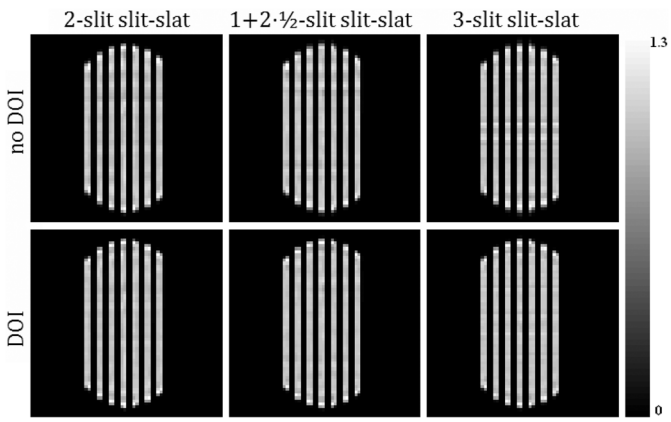

Fig. 17. Reconstructed images for the Defrise phantom simulated with different configurations of the slit-slat collimator, with (bottom row) and without (top row) DOI information.

compartments is slightly larger for the slit-slat configurations when compared to the pinhole ones. With the $5+2\cdot1/2$-pinhole collimator, increased blurring is seen at the centre of the phantom, in between the two rings. However, the inclusion of the DOI information in the reconstruction appears to reduce this blurring somewhat.

Fig. 18 and Fig. 19 show the reconstructed images simulated with and without DOI information for the Derenzo phantom, with different multi-pinhole and multi-slit slit-slat configurations, respectively. These are averaged over a section of 50 mm axially. For all configurations, 7 mm rods can be distinguished in the reconstructed images. In general, the pinhole collimators give better resolution, due to better angular sampling. The images simulated with DOI information present better resolution.

The reconstructed images for the simulations with the Zubal phantom are shown in Fig. 20 and Fig. 21, for the noise-free and noisy simulations, respectively. For the noise-free simulations, the reconstruction for the $5+2\cdot1/2$-pinhole shows slightly better transaxial and coronal images, specially in terms of structural definition and left-right symmetry, due to improved angular sampling. In the axial direction, the reconstructions with both collimators are comparable, even though the axial FOV is smaller for the $1+2\cdot1/2$-slit slit-slat. For the noisy simulations,

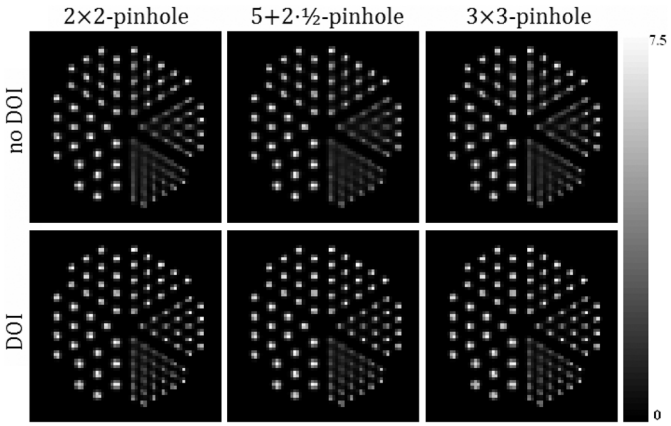

Fig. 18. Reconstructed images for the Derenzo phantom simulated with different configurations of the pinhole collimator, with (bottom row) and without (top row) DOI information.

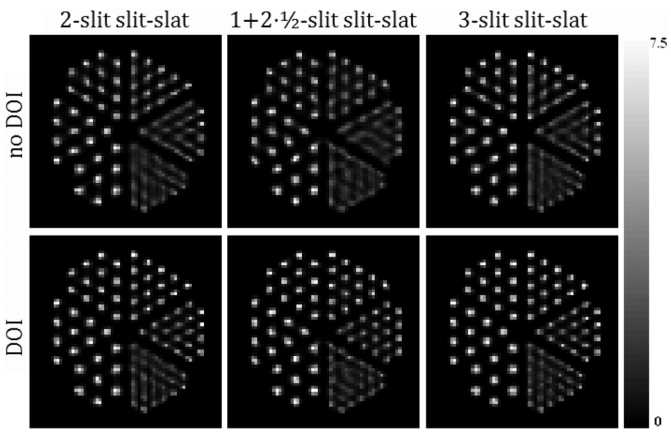

Fig. 19. Reconstructed images for the Derenzo phantom simulated with different configurations of the slit-slat collimator, with (bottom row) and without (top row) DOI information.

the $1 + 2 \cdot 1/2$-slit slit-slat image shows slightly less variability due to better statistics. However, it is difficult to draw a definite conclusion and more detailed evaluation is needed.

IV. Discussion

Fig. 11 and Fig. 12 show that improved efficiency is obtained for collimator configurations with multiple slits or pinholes when compared to the single-aperture configurations. Meaningful comparison with state-of-the-art SPECT systems is difficult as these utilise collimators designed to provide a compromise between sensitivity and resolution, e.g. for the Mediso Nucline X-Ring-4R 4-head SPECT, with LEHR collimators, resolution is better than 7 mm with a sensitivity of 2.7×10^{-4} cps/Bq. The proposed SPECT insert design can achieve similar sensitivity, albeit with a target resolution of 10 mm, but fitting within the MRI bore.

When the target resolution of the system is relaxed from 10 mm to 12 mm FWHM, there is a gain in sensitivity of about 30% (Fig. 11). Furthermore, as the intrinsic resolution of the detectors improves, so does the efficiency due to bigger pinhole/slit apertures, for the target resolution of the SPECT insert. The gain ranges between 10-30%, depending on the collimator

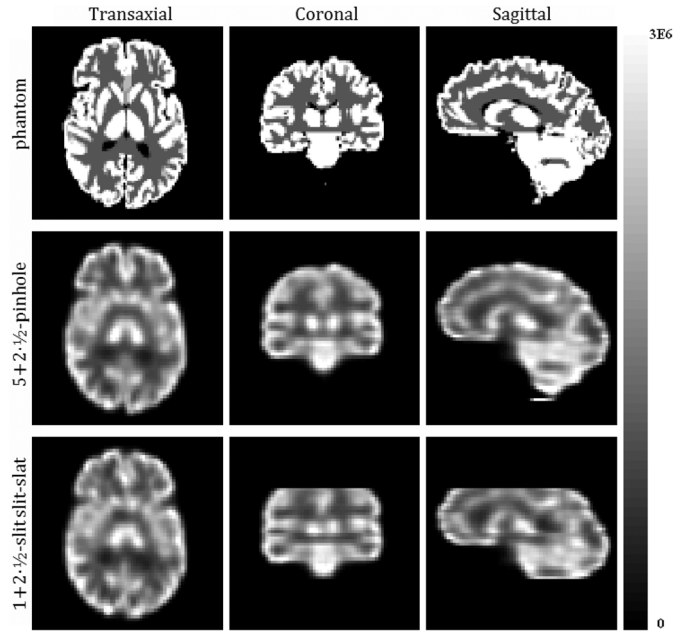

Fig. 20. Reconstructed images for the Zubal brain phantom simulated with the $1 + 2 \cdot 1/2$-slit slit-slat (bottom row) and $5 + 2 \cdot 1/2$-pinhole (middle row) collimators and excluding DOI information. The top row shows the brain phantom for comparison.

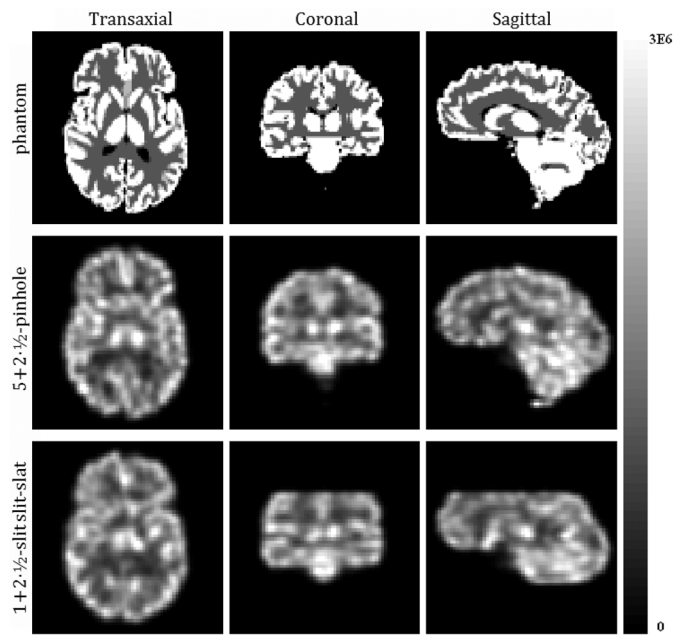

Fig. 21. Reconstructed images for the Zubal brain phantom simulated with noise and the $1 + 2 \cdot 1/2$-slit slit-slat (bottom row) and $5 + 2 \cdot 1/2$-pinhole (middle row) collimators and excluding DOI information. The top row shows the brain phantom for comparison.

configuration and R_i/R_t values. So we should aim for a lower intrinsic resolution, if possible, which also compensates for the minification. For all combinations of intrinsic and target resolutions, the slit-slat collimators achieve higher efficiency than the corresponding pinhole configurations. Note that with the slit-slat collimators, there is a reduction in sensitivity between the two detector rings due to the axial gap, but it does not reach zero.

Comparing the different multi-pinhole systems and the different multi-slit slit-slat systems, it would seem that the 2×2-pinhole and the 2-slit systems provide the best over-all performance, in terms of sensitivity (Fig. 11), uniformity (Fig. 15) and resolution (Fig. 16–19). However, there is a disadvantage with these designs from a practical point of view - the centre of the detector is used to image the edges of the object FOV and vice-versa. In practice, the performance of a detector tends to deteriorate towards the edges, so this is a sub-optimal situation. Therefore we would choose to avoid these designs and instead our preferred designs would be the $5 + 2 \cdot 1/2$-pinhole and the $1 + 2 \cdot 1/2$-slit slit-slat systems. These have better sensitivity than the 3×3-pinhole and 3-slit designs, respectively, and better uniformity in the absence of DOI. At this point we are not sure whether DOI information will be available.

Comparing the multi-pinhole to the multi-slit slit-slat collimators, the former gives better reconstructed uniformity and transaxial resolution, while the latter gives better axial resolution and higher sensitivity. The pinhole configurations have extended axial FOV but there is a risk of artefacts due to activity in incomplete sampled areas.

For the brain phantom (Fig. 20), reconstructions with the $5 + 2 \cdot 1/2$-pinhole collimator are slightly superior when compared to the $1 + 2 \cdot 1/2$-slit slit-slat, in terms of symmetry and accuracy of the activity distribution. However, the difference is reduced in the presence of noise due to the higher sensitivity of the slit-slat collimator (Fig. 21). For the slit-slat collimator, the reduced axial FOV may be a problem for tracers which require a reference region in the cerebellum, unless it is possible to reposition the patient in relation to the collimator's FOV.

In our system, the angular sampling is limited by the total number of detectors: 50 for the pinhole configurations and 25 for the slit-slat collimators, as each ring covers only half of the imaging FOV. This results in some degradation of image quality compared to a rotating system, where 128 projections are usually acquired over 360 degrees.

Regarding the use of DOI information, reconstructed images show reduced artefacts and improved uniformity in geometric phantoms. Future work includes exploration of anatomically-guided reconstruction algorithms to improve image quality.

V. Conclusion

The main goal of this paper was to discuss collimation design issues for a simultaneous SPECT/MRI brain scanner, using high-resolution detectors and prioritising sensitivity over spatial resolution.

Many of the constraints in the development of such collimators have been addressed, mainly the restricted space in the MRI bore and the angular sampling. Different types of multi-pinhole and multi-slit slit-slat collimators were designed and compared in terms of performance. Additionally new concepts of collimation were proposed to improve angular sampling: the half-pinhole and half-slit.

The rotation of one ring in regards to the other is a simple solution for improved angular sampling for the multi-pinhole systems. The use of DOI information has the potential to improve the reconstructed image quality.

Comparing the multi-pinhole and multi-slit slit-slat collimators, the former gives better reconstructed uniformity and transaxial resolution, while the latter gives better axial resolution and sensitivity. Regarding individual configurations, the 2×2-pinhole and 2-slit slit-slat designs achieved relatively high sensitivity, but would have the disadvantage of a sub-optimal utilisation of the detector area. As a result, the $5 + 2 \cdot 1/2$-pinhole and $1 + 2 \cdot 1/2$-slit slit-slat designs are preferable. Further evaluation is needed with prototype collimators.

References

[1] E. Breton, P. Choquet, C. Goetz, J. Kintz, P. Erbs, R. Rooke, and A. Constantinesco, "Dual SPECT/MR imaging in small animal," *Nucl. Instrum. Methods Phys. Res. A*, vol. 571, no. 1–2, pp. 446–448, 2007.

[2] C. Goetz, E. Breton, P. Choquet, V. Israel-Jost, and A. Constantinesco, "SPECT low-field MRI system for small-animal imaging," *J. Nucl. Med.*, vol. 49, no. 1, pp. 88–93, 2007.

[3] D. Meier, D. Wagenaar, S. Chen, J. Xu, J. Yu, and B. Tsui, "A SPECT camera for combined MRI and SPECT for small animals," *Nucl. Instrum. Methods Phys. Res. A*, vol. 652, no. 1, pp. 731–734, 2011.

[4] B. M. W. Tsui, J. W. Hugg, J. Xu, S. Chen, D. Meier, W. A. Edelstein, A. El-Sharkaway, D. J. Wagenaar, and B. E. Patt, N. J. Pelc, E. Samei, and R. M. Nishikawa, Eds., "Design and development of MR-compatible SPECT systems for simultaneous SPECT-MR imaging of small animals," *Proc. SPIE*, vol. 7961, pp. 79 611Y:1–7, 2011.

[5] M. J. Hamamura, S. Ha, W. W. Roeck, L. T. Muftuler, D. J. Wagenaar, D. Meier, B. E. Patt, and O. Nalcioglu, "Development of an MR-compatible SPECT system (MRSPECT) for simultaneous data acquisition," *Phys. Med. Biol.*, vol. 55, no. 6, pp. 1563–75, 2010.

[6] P. Busca, C. Fiorini, A. D. Butt, M. Occhipinti, R. Peloso, R. Quaglia, F. Schembari, P. Trigilio, G. Nemeth, P. Major, K. Erlandsson, and B. F. Hutton, "Simulation of the expected performance of INSERT: A new multi-Modality SPECT/MRI system for preclinical and clinical imaging," *Nucl. Instrum. Methods Phys. Res. A*, vol. 734, pp. 141–6, 2014.

[7] P. Busca, C. Fiorini, A. D. Butt, M. Occhipinti, R. Quaglia, P. Trigilio, G. Nemeth, P. Major, T. Bukki, K. Nagy, C. Piemonte, A. Ferri, A. Gola, J. Rieger, and T. Niendorf, "Development of a high-resolution detection module for the INSERT SPECT/MRI system," *EJNMMI Phys.*, vol. 1, p. A24, 2014, Suppl 1.

[8] R. K. Rowe, J. N. Aarsvold, H. H. Barrett, J.-C. Chen, W. P. Klein, B. A. Moore, I. W. Pang, D. D. Patton, and T. A. White, "A stationary hemispherical SPECT imager for three-dimensional brain imaging," *J. Nucl. Med.*, vol. 34, no. 3, pp. 474–80, 1993.

[9] L. R. Furenlid, D. W. Wilson, Y.-C. Chen, H. Kim, P. J. Pietraski, M. J. Crawford, and H. H. Barrett, "FastSPECT II: A second-generation high-resolution dynamic SPECT imager," *IEEE Trans. Nucl. Sci.*, vol. 51, no. 3, pp. 631–35, Jun. 2004.

[10] F. J. Beekman and B. Vastenhouw, "Design and simulation of a high-resolution stationary SPECT system for small animals," *Phys. Med. Biol.*, vol. 49, no. 19, pp. 4579–92, 2004.

[11] J. Xu, S. Chen, J. Yu, D. Meier, D. J. Wagenaar, B. E. Patt, and B. M. W. Tsui, "SPECT data acquisition and image reconstruction in a stationary small animal SPECT / MRI System," *Proc. SPIE*, vol. 7622, pp. 1–8, 2010.

[12] K. Van Audenhaege, S. Vandenberghe, K. Deprez, B. Vandeghinste, and R. Van Holen, "Design and simulation of a full-ring multi-lofthole collimator for brain SPECT," *Phys. Med. Biol.*, vol. 58, no. 18, pp. 6317–36, 2013.

[13] L. Cai, X. Lai, Z. Shen, C.-T. Chen, and L.-J. Meng, "MRC-SPECT: A sub-500um resolution MR-compatible SPECT system for simultaneous dual-modality study of small animals," *Nucl. Instrum. Methods Phys. Res. A*, vol. 734, pp. 147–51, 2014.

[14] S. T. Mahmood, K. Erlandsson, I. Cullum, and B. F. Hutton, "Design of a novel slit-slat collimator system for SPECT imaging of the human brain," *Phys. Med. Biol.*, vol. 54, no. 11, pp. 3433–3449, 2009.

[15] J. R. Mallard and M. J. Myers, "The performance of a gamma camera for the visualization of radioactive isotopes in vivo," *Phys. Med. Biol.*, vol. 8, no. 2, pp. 165–82, 1963.

[16] S. D. Metzler, R. Accorsi, A. S. Ayan, and R. J. Jaszczak, "Slit-slat and multislit-slat collimator design and experimentally acquired phantom images from a rotating prototype," *IEEE Trans. Nucl. Sci.*, vol. 57, no. 1, pp. 125–34, Feb. 2010.

[17] R. Accorsi and S. D. Metzler, "Analytic determination of the resolution-equivalent effective diameter of a pinhole collimator," *IEEE Trans. Med. Imag.*, vol. 23, no. 6, pp. 750–63, 2004.
[18] S. D. Metzler and R. Accorsi, "Resolution- versus sensitivity-effective diameter in pinhole collimation: Experimental verification," *Phys. Med. Biol.*, vol. 50, no. 21, pp. 5005–17, 2005.
[19] R. Accorsi, J. R. Novak, A. S. Ayan, and S. D. Metzler, "Derivation and validation of a sensitivity formula for slit-slat collimation," *IEEE Trans. Med. Imag.*, vol. 27, no. 5, pp. 709–22, 2008.
[20] A. Bousse, K. Erlandsson, N. Fuin, D. Salvado, and B. F. Hutton, "Variance prediction in SPECT reconstruction based on the fisher information using a novel angular blurring algorithm for computation of the system matrix angular rebinning for geometry independent SPECT reconstruction," in *Proc. IEEE Nuclear Science Symp. and Medical Imaging Conf.*, 2013, pp. 1–6.
[21] H. M. Hudson and S. Larkin, "Accelerated image reconstruction using ordered subsets of projection data," *IEEE Trans. Med. Imag.*, vol. 13, pp. 601–609, 1994.
[22] I. G. Zubal, C. R. Harrel, E. O. Smith, Z. Rattner, G. Gindi, and P. B. Hoffer, "Computerized three-dimensional segmented human anatomy," *Med. Phys.*, vol. 21, no. 2, pp. 299–302, 1994.